Title	Modelling fluid induced seismicity on a nearby active fault
Authors(s)	Murphy, Shane, O'Brien, G. S., McCloskey, J., Bean, Christopher J., Nalbant, S.
Publication date	2013-09
Publication information	Murphy, Shane, G. S. O’Brien, J. McCloskey, Christopher J. Bean, and S. Nalbant. “Modelling Fluid Induced Seismicity on a Nearby Active Fault.” Oxford University Press, September 2013. https://doi.org/10.1093/gji/ggt174.
Publisher	Oxford University Press
Item record/more information	http://hdl.handle.net/10197/5430
Publisher's statement	This article has been accepted for publication in Geophysical Journal International ©:The Authors 2013. Published by Oxford University Press on behalf of The Royal Astronomical Society. All rights reserved.
Publisher's version (DOI)	10.1093/gji/ggt174

Geophysical Journal International

Geophys. J. Int. (2013) doi: 10.1093/gji/ggt174

Geophysical Journal International Advance Access published May 22, 2013

Modelling fluid induced seismicity on a nearby active fault

S. Murphy,[1] G. S. O'Brien,[2] J. McCloskey,[1] C. J. Bean[3] and S. Nalbant[1]

[1] *School of Environmental Sciences, University of Ulster, Co. Derry, Northern Ireland. E-mail: s.murphy@ulster.ac.uk*
[2] *Tullow Oil plc, Geophysical Technology Group, Leopardstown, Dublin 18, Ireland*
[3] *School of Geological Sciences, UCD, Dublin, Ireland*

Accepted 2013 April 26. Received 2013 April 25; in original form 2012 November 01

SUMMARY

We present a numerical investigation of the effect that static stress perturbations due to fluid injection have on a nearby active fault where the fluid does not come in physical contact with the fault. Our modelling employs a lattice Boltzmann pore diffusion model coupled with a quasi-dynamic earthquake rupture model. As diffusivities and frictional parameters can be defined independently at individual nodes/cells this allows us to replicate complex 3-D geological media in our simulations. We demonstrate the effect an injection can have on an active nearby fault. Compared with our control catalogue (identical to the original simulation but without the injection), the injection not only altered the timing of the next earthquake sequence, it also changed its size, producing a M_w 6.7 event, the largest observed earthquake on the fault. This large event pushes the fault into a subcritical state from which it took roughly 200 yr of continuous tectonic loading for the fault to return to a critical state.

Key words: Numerical approximations and analysis; Self-organization; Permeability and porosity; Friction; Seismicity and tectonics; Computational seismology.

1 INTRODUCTION

In terms of mechanics, fluid injection can induce seismicity either through increasing pore fluid pressure in the volume and thereby reducing the effective normal stress on a target fault or by direct deformation of the rock volume which changes the Coulomb stress on all the faults in the volume. In the first case, assuming low permeability, which exists in fracking, for example, seismicity is localized to the immediate vicinity of the injection plume. In the second case, the Coulomb stress perturbations extend over a much larger spatial scale affecting faults outside the reach of the injection plume.

To date, numerical simulations simulating induced seismicity have focused on investigating the seismic response due to the physical presence of fluids on the fault plane (i.e. Baisch *et al.* 2010; McClure & Horne 2011; Cappa & Rutqvist 2012). In this paper, we outline a technique that simulates the effect that fluid injection has on nearby faults located outside the fluid plume. While this phenomenon is rarely considered in the context of induced seismology, it could explain earthquakes near injection site whose focal mechanisms contain no volumetric change. Possible examples of this type of induced seismicity could be the events observed in the Paradox Valley, Colorado (Ake 2005; i.e. Baisch *et al.* 2010; McClure & Horne 2011; Cappa & Rutqvist 2012) and Ashtabula, Ohio (Seeber *et al.* 2004).

In purely tectonic environments, it has been shown that small static stress changes produced by one earthquake can trigger subsequent earthquakes on surrounding faults (Stein 1999; McCloskey *et al.* 2005; Nalbant *et al.* 2005; Toda *et al.* 2005). Studies using more complex rate-and-state friction laws have revealed a more complicated relationship between homogeneous stress changes and the advancement/retardation of the timing of the next earthquake on a fault (Perfettini *et al.* 2003; Gallovič 2008). Remote stress perturbations due to fluid injections are inherently more complicated than the homogeneous stress changes due to greater complexity in the temporal and spatial variability across the fault depending on the pumping scenario, reservoir characteristics and relative fault-injection location. We use the terms 'remote stress perturbations' and 'remotely induced seismicity' as we are solely modelling the stress perturbations caused by the fluid, which does not physically reach the fault plane. To model this remotely induced seismicity we will examine the static stress perturbations produced by a given injection scenario on a nearby isolated fault.

2 METHOD

Our aim is to produce a numerical model that is computationally fast but at the same time retains as much fluid and rock physics as possible. Subsurface fluid flow is simulated by solving the pore pressure diffusion equation using a 3-D Lattice Boltzmann method (LB) (Qian &

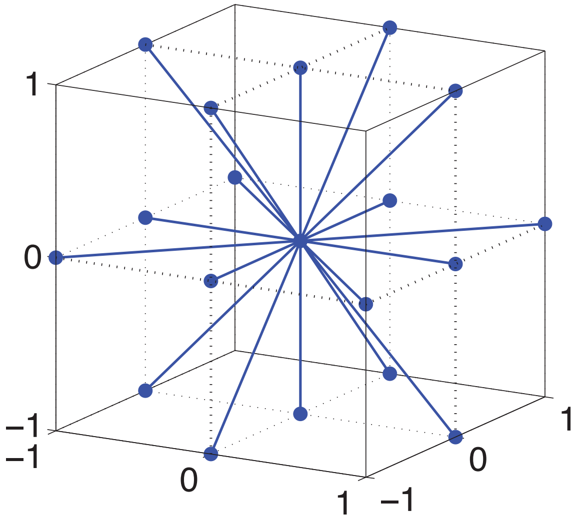

Figure 1. D3Q19 lattice geometry model used in the Lattice Boltzmann pore pressure simulations.

d'Humieres 1992; Zheng & Shu 2006) allowing us to model heterogeneous subsurface structures if necessary. Seismicity is modelled with a rate-and-state friction law using a 3-D quasi-dynamic (QD) relationship between stress and slip (Rice & Ben-Zion 1996; Perfettini & Schmittbuhl 2003; Gallovič 2008) with a modified rate-and-state ageing friction law (Dieterich 1979; Ruina 1983; Linker & Dieterich 1992). In the next two subsections we describe the construction of the pore diffusion and seismicity models separately as well as a description of the interaction between the two models.

2.1 Fluid injection

Taking p as the pore pressure, and $\boldsymbol{D}$ as the diffusion tensor at position vector ξ, the pore diffusion equation to be solved is defined as

$$\frac{\partial\, p(\xi,t)}{\partial\, t} = \frac{\partial}{\partial \xi_i}\left(D_{ij}\frac{\partial p(\xi,t)}{\partial \xi_j}\right). \tag{1}$$

We will use the convention that $\mathbf{x}$ is a 3-D spatial vector that describes a position on the fault plane, while ξ describes a position in the 3-D injection volume. Diffusivities can be related to the permeability tensor $\boldsymbol{K}$ through the equation:

$$K_{ij} = \phi\,\eta\,\beta_{\mathrm{f}}\,D_{ij}, \tag{2}$$

where ϕ porosity, η the viscosity and β_{f} the fluid compressibility. We have expanded the 2-D LB method of Maillot & Main (1996) to 3-D using the D3Q19 lattice geometry defined by the velocity vectors depicted in Fig. 1. To convert the 2-D equations to 3-D, the nearest neighbours were increased from $b = 4$ or 6 (in the case of a square or triangular grids, respectively) to $b = 19$, with the normalization factors for a D3Q19 lattice defined as (Qian & d'Humieres 1992):

$$t_i = \begin{cases} {}^1\!/_3 & i = 0 \\ {}^1\!/_{18} & 1 \le i \le 6 \\ {}^1\!/_{36} & 7 \le i \le 18 \end{cases}, \tag{3}$$

where i is the index of the directional vector. This methodology allows us to define the diffusivity tensor at each point in the model volume, meaning that it can potentially simulate complicated anisotropic fluid diffusion in a heterogeneous medium.

2.2 Induced seismicity

Splitting a fault into discrete elemental blocks (or discrete points), the acceleration for each element/point can be defined quasi-dynamically using the equation (Rice 1993; Perfettini *et al.* 2003; Gallovič 2008):

$$\dot{v}(\mathbf{x},t) = \frac{\int_{\Sigma} K^{\tau}(\mathbf{x},\mathbf{x}')(v(\mathbf{x}',t) - V_{\mathrm{pl}})\mathrm{d}\mathbf{x}' - \dfrac{b(\mathbf{x})\,\dot{\theta}(\mathbf{x},t)\,\sigma_{\mathrm{n}}(\mathbf{x},t)}{\theta(\mathbf{x},t)} - \mu(\mathbf{x},t,v(\mathbf{x},t),\theta(\mathbf{x},t))\,\dot{\sigma}_{\mathrm{n}}(\mathbf{x},t) + \dot{\tau}^{E}(\mathbf{x},t)}{\dfrac{a(\mathbf{x})\,\sigma_{\mathrm{n}}(\mathbf{x},t)}{v(\mathbf{x},t)} + \dfrac{G}{2\,\beta}}. \tag{4}$$

The dot denotes the temporal derivative, v is the slip velocity, V_{pl} is the long-term plate velocity loading the fault, θ is the state variable, σ_{n} is the normal stress, a and b rate and state frictional parameters, β is the shear wave velocity, G is the shear modulus. μ is the rate and state coefficient of friction whose value is dependent on slip velocity and state (Dieterich 1979; Ruina 1983) and is given as:

$$\mu(\mathbf{x}, t, v(\mathbf{x}, t), \theta(\mathbf{x}, t)) = \mu^* + a(\mathbf{x}) \log \left[\frac{v(\mathbf{x}, t)}{v^*} \right] + b(\mathbf{x}) \log \left[\frac{\theta(\mathbf{x}, t)\, v_*}{d_c} \right], \tag{5}$$

where μ^* and v^* are the reference coefficient of friction and slip rate. $a(\mathbf{x})$and $b(\mathbf{x})$ are frictional parameters that govern whether the cells slip aseismically (i.e. $a(\mathbf{x}) - b(\mathbf{x}) > 0$) or seismically ($a(\mathbf{x}) - b(\mathbf{x}) < 0$). As demonstrated by Blanpied *et al.* (1991), the frictional relationship $a-b$ varies with temperature and therefore depth; for this reason we allow the frictional parameters a and b to vary spatially, this will be discussed in more detail in the next section. d_{c} is the characteristic slip distance which we assume is constant across the whole fault.

K^{τ} is the shear stiffness kernel and $\dot{\tau}^{E}$ is the shear stressing rate due to external influences. Variations in the normal stress are accounted for by:

$$\dot{\sigma}_{\mathrm{n}}(\mathbf{x}, t) = \int_{\Sigma} K^{\sigma_{\mathrm{n}}}(\mathbf{x}, \mathbf{x}')(v(\mathbf{x}', t) - V_{\mathrm{pl}})\, d\mathbf{x}' + \dot{\sigma}_{\mathrm{n}}^{E}(t), \tag{6}$$

where $K^{\sigma_{\mathrm{n}}}$ is the stiffness kernel for changes in the normal stress due to slip by other elements on the fault plane (in the case of a vertical fault this is a null matrix). $\dot{\sigma}_{\mathrm{n}}^{E}$ is the rate of change of the normal stress due to external influences, for the simulations presented in this paper the external influence is due to the stress perturbations caused by the injection of a fluid near a fault (the fluid, however does not make contact with the fault). $\dot{\sigma}_{\mathrm{n}}^{E}$ and $\dot{\tau}^{E}$ are determined by:

$$\dot{\tau}^{E}(\mathbf{x}, t) = \int_{V_{\mathrm{inj}}} K_{\mathrm{inj}}^{\tau}(\mathbf{x}, \xi)\, p(\xi, t)\, d\xi \tag{7}$$

$$\dot{\sigma}_{\mathrm{n}}^{E}(\mathbf{x}, t) = \int_{V_{\mathrm{inj}}} K_{\mathrm{inj}}^{\sigma_{\mathrm{n}}}(\mathbf{x}, \xi)\, p(\xi, t)\, d\xi. \tag{8}$$

The stiffness matrices in eqs (4), (6)–(8) (i.e. K^{τ}, $K^{\sigma_{\mathrm{n}}}$, K_{inj}^{τ}, $K_{\mathrm{inj}}^{\sigma_{\mathrm{n}}}$) are all calculated using analytical solutions for static slip dislocations/pressure changes in an elastic half space (Okada 1992). In the case of $K^{\sigma_{\mathrm{n}}}$ and K^{τ} the stiffness kernels relate to dip-slip or strike-slip sources (depending on the type of fault). For stress perturbations due to fluid injection the source features for $K_{\mathrm{inj}}^{\sigma_{\mathrm{n}}}$ and K_{inj}^{τ} are modelled as inflationary/deflationary point sources. The differential change in the external shear and normal stress (due to the pressure changes in the reservoir) between time steps in the LB simulation are integrated as a sine function with the limits of the temporal integral dependant on the time step in the QD rupture model. Our model is a one way coupled system whereby pore pressure changes alter conditions on the fault but slip on the fault does not affect pore pressure or diffusivity in the reservoir. An important assumption we make is that the injected fluid does not directly interact with the fault (i.e. lowering effective normal stress directly) nor does it affect the geo-mechanical stability of the reservoir.

For the evolution of the state variable in eq. (4), a state law which accounts for temporal variations of normal stress was used (Linker & Dieterich 1992):

$$\dot{\theta}(\mathbf{x}, t) = 1 - \frac{v(\mathbf{x}, t)}{d_c} - \alpha \frac{\theta(\mathbf{x}, t)\, \dot{\sigma}_{\mathrm{n}}(\mathbf{x}, t)}{b(\mathbf{x})\, \sigma_{\mathrm{n}}(\mathbf{x}, t)}. \tag{9}$$

d_{c} and b are the same frictional parameters defined in eq. (5). α is a laboratory derived parameter and is set to 0.2 as suggested by Perfettini *et al.* (2003) and Linker & Dieterich (1992); a value derived from experimental data. However, we found in cases where b is near zero, eq. (8) can become unstable as the state variable can become dominated by the third term in eq. (8), especially in cases where the normal stress is small (i.e. close to the free surface) and the fault is dipping. For this reason, we set α to zero when b is zero. Eqs (4), (6) and (9) are solved using a Runga-Kutta technique with an adaptive time step (Press *et al.* 1992) which increases computational efficiency. During the injection period, the time step used in the QD model is constrained to be less than the time step used in the LB simulation. Permeability changes related to fault slip could be included but any relationship would have to be defined from empirical studies and we have omitted this in the current study.

2.3 Earthquake catalogue

Earthquakes occur in the model when any cell on the fault slips faster than 1 mm s^{-1}. This velocity is smaller than the limit taken by Perfettini *et al.* (2003) but it is inside the limits set by Roy & Marone (1996). During an earthquake the program keeps track of the amount of seismic slip (i.e. slip that occurred while the corresponding cell had a velocity above 1 mm s^{-1}) on the fault. At the end of the event, the moment M_0, in Nm, is calculated using:

$$M_o = G\, \mathrm{d}x^2 \sum_{i=1}^{N} \delta_{\mathrm{s}}(i), \tag{10}$$

where G is the shear modulus, dx is the cell size, δ_s is the seismic slip in cell i and N is the number of cells whose slip velocity is greater than 1 mm s^{-1}. From the moment, the magnitude is calculated based on (Hanks & Kanamori 1979):

$$M_w = \frac{2}{3}\left(\mathrm{Log}\left(M_o\right) - 9.1\right). \tag{11}$$

Using this definition for an earthquake, we can model remotely induced seismicity on complex faults due to complicated injection situations using the coupled LB – QD model.

3 MODEL SETUP

We will now use the coupled model to investigate how pore pressure changes during a injection affects a nearby fault in an active tectonic setting. As this is a general study, the model is generic and not meant to be indicative of any particular injection type or fault.

The QD model is defined on a 40 km by 20 km strike-slip fault with a 60° dip. The fault is loaded by a plate velocity of 35 mm yr^{-1}, which would be equivalent to a high strain environment found at active plate boundaries (Lisowski *et al.* 1991). Fig. 2 illustrates the relative location of the fault plane to the site of injection which takes place roughly midway along the strike of the fault.

The frictional a and b parameters in the rate and state friction are varied spatially to produce earthquakes of variable sizes inside a seismogenic zone with a finite width. A depth dependent variation to the rate-and-state a and b parameters as defined by Rice (1993) is used to produce a negative $a-b$ value over the depth range of 2–14.3 km allowing seismic events in this zone. Simulations using solely this spatial variation (whereby the negative $a-b$ is smooth over the seismogenic layer) produce near-periodic characteristic earthquakes (Rice 1993; Perfettini *et al.* 2003). In reality, faults produce a power-law scaling relationship between an earthquake's magnitude and its frequency of occurrence, a feature, which is absent in these 'smooth' $a-b$ spatial distributions. Hillers *et al.* (2006) demonstrated that adding a random spatial variation to d_c to account for geometric heterogeneity leads the fault to produce a rich range of event size and locations, a feature not observed in the smoothly varying frictional models previously described. In our numerical model we combine the depth dependent change in the frictional parameter a (used to reproduce a seismogenic zone) with a spatial fractal variation. We choose to vary a rather than d_c to add a variability to the recurrence time to different patches on the fault [a function which is dependent on the $a-b$ parameter and not d_c (Barbot *et al.* 2012)]. d_c remains constant across the fault in this model while b varies only with depth as defined by Rice (1993) giving it a constant value of 0.019 between 4 and 13 km (above and below this zone b smoothly decreases to 0.0175 and 0, respectively). In comparing our results to those of Hillers *et al.* (2006) we find that the spatial variation of either frictional parameter produces similar results in terms of generating variable frequency—size relationships. The spatial variance of a is characterized in our model by the following equation:

$$a(x, z) = a_r(z) + (a_f(x, z) - 0.5) * \upsilon, \tag{12}$$

where x and z define position along strike and depth on the fault respectively, a_r is the depth dependent variability of a derived by Blanpied *et al.* (1991) which allows the definition of a seismogenic zone on the fault. a_f is a 2-D fractal distribution normalized to range between 0 and 1. υ is a measure of fault roughness which is set to 0.005 so that the depth dependent variability (i.e. a_r) is larger than the fractal variability meaning that the macroscopic and deterministic definition of shallow and deep aseismic zones surrounding the seismogenic region, is still the

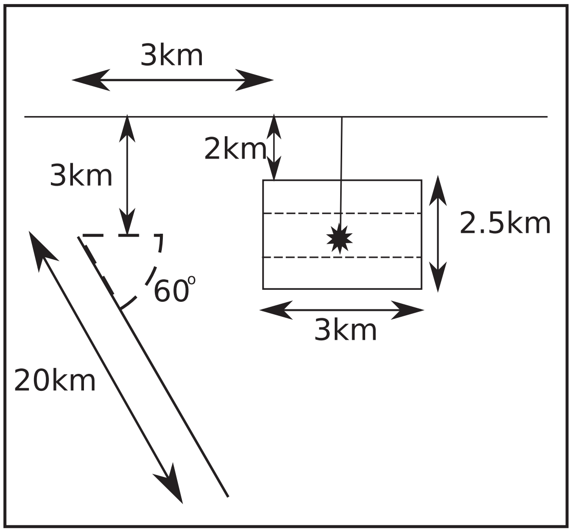

Figure 2. Cross-section schematic of the injection site relative to the fault used in the case study. The injection is occurring approximately half way along the strike length of the fault which is 40 km long. The injection takes place at a depth of 3.3 km (denoted by the star) into a reservoir with a depth range of 3–4.5 km. The horizontal dashed lines above and below the injection represent the boundary between the Reservoir layer and Cap Layers 1 and 2 (the diffusivities of which are defined in Table 2, the same boundary is represented by blue lines in Fig. 5). The solid line which makes a box around the injection is the edge of the LB model, it has very low diffusivity (called as 'Boundary' in Table 2 and is denoted by the red lines in Fig. 5).

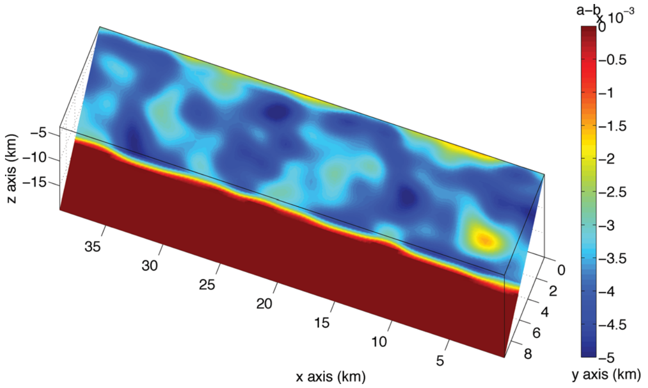

Figure 3. The spatial variation of the frictional parameter $a - b$ across the fault plane. Where $a - b < 0$ the fault exhibits stick–slip behaviour, and aseismic slip when $a - b > 0$. Using a variable $a - b$, which is negative for the depth range of 2–14.3 km (Rice 1993). A small amplitude (±0.005) fractal roughness was added in order to produce some heterogeneity to the fault. The $a - b$ values displayed are the absolute values with an apparent mean value of -0.0038 in the stick–slip section of the fault (i.e. the predominantly blue section of the fault). The colour bar saturates at $a - b = 0$, therefore any dark red areas denote velocity strengthening (i.e. aseismic) patches on the fault.

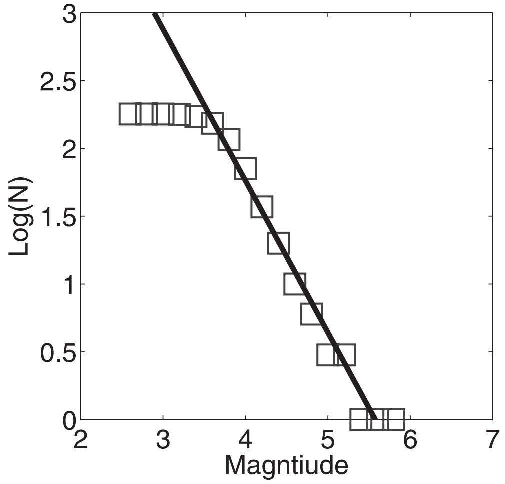

Figure 4. Frequency-size distribution for 100 yr of seismicity on the fault prior to the injection (i.e. from year 400 to 500). The best-fit slope was calculated over the magnitude range of 3.8–5.8 and has a slope of -1.1 and y intercept value of 6.09.

dominant frictional feature on the fault (see Fig. 3). Between the depth range of 4–13 km, where traditionally $a = 0.015$ (i.e. $a–b = -0.004$), the apparent mean value of the fractal distribution in this zone is $a = 0.0152$ (i.e. $a–b = -0.0038$), with an apparent standard deviation of 5.37×10^{-4}. Therefore the fault is dominantly velocity weakening in the depth range 3–14.2 km and velocity strengthening below 14.2 km (in Fig. 3 the colour bar is saturates at $a–b = 0$, therefore any red areas denote velocity strengthening patches on the fault which extends to a depth of 17.3 km).

The variation means that the critical cell stiffness is no longer constant in the seismogenic section of the fault. In the simulations presented in this paper the ratio of cell size to critical cell size (i.e. the h/h^* ratio) varies with its largest value being 0.52 (Table 3). This means that small patches of the fault may potentially be acting discretely (Rice 1993; Hillers *et al.* 2006).

The fault is initially loaded tectonically for 500 yr so as to build up a heterogeneous slip-rate and state distribution across the fault plane as well as tectonically loading the fault. By 500 yr the fault has been through 10 seismic sequences (i.e. the fault has an approximate quasi-periodic recurrence time of 50 yr). The seismicity in the 100 yr prior to the injection has a Gutenberg-Richter scaling of the frequency size-distribution with a slope of -1.1 (see Fig. 4). The smallest earthquake that the QD model can generate is based on the cell size and the smallest nucleation size that the fault can accommodate. As the cell size is smaller than the nucleation size, the nucleation length will constrain the smallest earthquake size. There are different definitions for the nucleation length, we found the definition that best fit our results is (Rice 1993) :

$$L = \frac{2\,G\,d_c}{\pi\ \max[b - a]\,\sigma_n}, \tag{13}$$

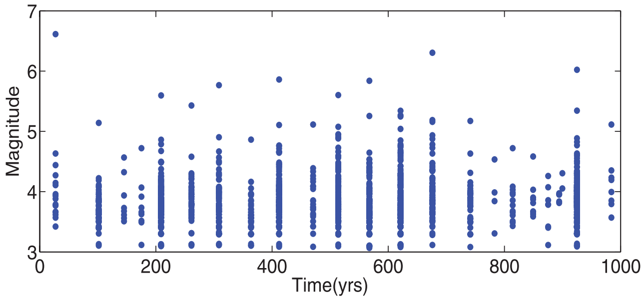

Figure 5. The seismicity generated by the QD model over 1000 yr with no fluid injection, in which time the largest earthquake observed was a 6.6 M_w in year 27.

Table 1. Parameters used in LB pore diffusion modelling.

Parameter	Value
dx (m)	100
dt (s)	50
No. of nodes	30 × 30 × 25
Duration (d)	15

where d_c is the critical slip distance, G is the shear modulus, max[$b-a$] is the maximum value of the frictional parameters a and b, σ_n is the effective normal stress. Taking $d_c = 0.02$ m, $G = 30$ GPa, max[$b-a$] = 0.0051; $\sigma_n = 100$ MPa gives a nucleation length of roughly 764 m. Using the empirical relationship between the average stress drop ($\Delta\sigma$) and slip (δ) (Scholz 2002)

$$\delta = \frac{\Delta\sigma}{G} L, \tag{14}$$

where L is the length of the slipping region, this can be combined with the definition of the seismic moment to give

$$M_o = \Delta\sigma\, L^3. \tag{15}$$

The moment can be converted to magnitude using eq. (10). The stress drop in models using rate-and-state friction laws can be approximated using

$$\Delta\sigma = (b-a)\,\sigma_n \ln\left[\frac{v_{\text{rupt}}}{v_{\text{int}}}\right], \tag{16}$$

where the slip velocity during an earthquake is $v_{\text{rupt}} \approx 1$ m s^{-1}, and that during the interseismic time slip velocity is roughly $v_{\text{int}} \approx 10^{-10}$ m s^{-1} (Barbot *et al.* 2012). The normal stress is $\sigma_n = 100$ MPa for majority of the fault whilst $b-a$ varies between: 0.0051 and 0.0015 in the seismogenic zone which is taken between a depth of 4–13 km. Substituting these values into eq. (16) gives a static stress drop range between 8.2 and 2.4 MPa per cell which is inside expected average stress drop range of real earthquakes [i.e. 0.03–30 MPa (Scholz 2002)] with an average stress drop of 6.2 MPa (based on the mean $b-a$ value of 0.0038). Taking the smaller stress drop (i.e. 2.4 MPa) the magnitude of the smallest earthquake should be roughly M_w 3.95.

The maximum magnitude that the fault can support is proportional to the seismogenic zone. Using the average stress drop (i.e. 6.2 MPa) and setting $L = 13$ km (i.e. the seismogenic width of the fault) or 40 km (i.e. the length of the fault) in eq. (15) gives a magnitude range of $M_w =$ 6.7–7.7. As can be seen in Fig. 5 our approximations overestimates the size of both the smallest and largest earthquakes observed over a 1000 yr period (in a simulation with no injection) where the biggest and smallest earthquakes were M_w 6.6 and 3.1, respectively. Consequentially the injection cannot induce very small earthquakes on the fault and thus does not model the full amount of induced seismicity.

The injection takes place into a permeable planar layer with a thickness of 1.5 km with less permeable layers above and below it and an impermeable layer defining the model boundary (see Table 2 and Fig. 6). This constrains the majority of the fluid to spread only inside the model and gives the reservoir a volumetric size of 6 km^3. There is some small diffusion occurring in the impermeable layer meaning the reservoir acts as a fluid trap but is not a perfectly closed system. We assume that the diffusivity is homogeneous in each of the layers. In

Table 2. Parameters used for pore diffusion simulation. These values are within the general range of permeable basalts, fractured igneous rocks, sandstones/siltstones and intact carbonates (Roeloffs 1996).

Strata	D_{xx} (m^2 s^{-1})	D_{yy} (m^2 s^{-1})	D_{zz} (m^2 s^{-1})
Cap Layer 1	0.1	0.1	0.1
Reservoir	2.0	2.0	0.1
Cap Layer 2	0.1	0.1	0.1
Boundary	0.05	0.05	0.1

Table 3. Parameters with spatially constant values used in the QD model. h/h^* is ratio of cell size to critical cell size. dx is the spatial distance between cell centres. α is the additional constant required by the modified Ageing State Law the value used is based on laboratory experiments (Linker & Dieterich 1992).

Parameter	Value	Parameter	Value	Parameter	Value
G (GPa)	30	V^* (m s^{-1})	10^{-6}	dx (m)	400
d_c (m)	0.02	μ^*	0. 6	dt (s)	Variable
α	0.2	h/h^*	0.52	No. of cells	50 × 100

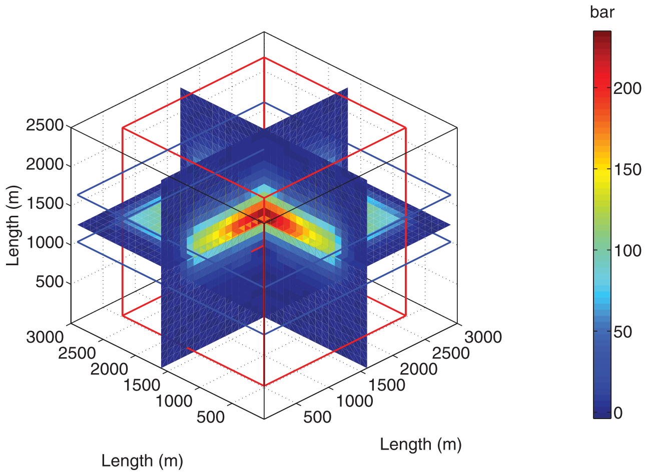

Figure 6. Pressure (in bars) snapshot during injection in the LB pore pressure simulation. Blue squares define the top and bottom of the reservoir layer. Red lines define a cube which represents the boundary of an all encompassing impermeable layer.

reality, this is not the case. We justify this simplification as we are examining the effect of stress perturbations caused by the injection at a distance from the reservoir, not in it. Therefore, the variability of stress perturbation across the fault caused by the diffusivity heterogeneity in the reservoir would be smoothened with increasing distance between injection site and fault. Our assumption is therefore that the change in stress perturbations caused by small amplitude variations in diffusivities within the individual layers would be small relative to the global stress change observed by distant fault patches.

A pore pressure point source at the centre of the injection model is used to replicate fluid injection into the reservoir layer. This takes place at a depth of 3 km. The injection is initiated at the start of year 501 and runs for 6.37 days; the temporal variation in pumping rate during this time is depicted in Fig. 7. The pore diffusion simulation runs for 15 days in total (see Table 1).

To ascertain the effect that the injection has on the seismicity, two model runs are required. One where the stress perturbations due to the injection are included, the second, termed the 'control catalogue' is produced by running an identical simulation but with no injection taking place in it.

4 RESULTS AND DISCUSSION

During the period of the injection, 24 events occur on the fault. The fact that the earthquake sequence occurs during the injection is also not uncommon, Nicol *et al.* (2011) observed that in 70 per cent of the injection/extraction induced seismicity cases they examined the earthquakes

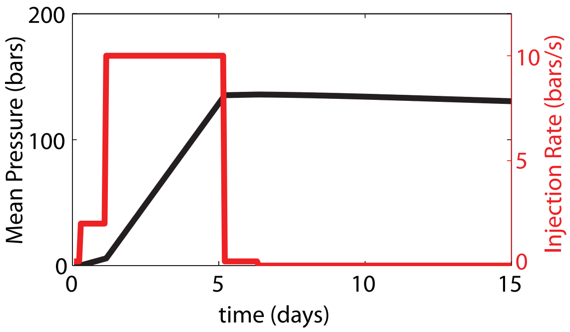

Figure 7. Pressure injection history. Maximum injection rate (red line) is 10 Bar s^{-1}. Injection stops at 6.73 d. Mean pressure (black line) is for the whole simulation volume not just the reservoir. After the end of the injection there is slight decrease in mean pressure with time that is due to some diffusion occurring in the impermeable boundary.

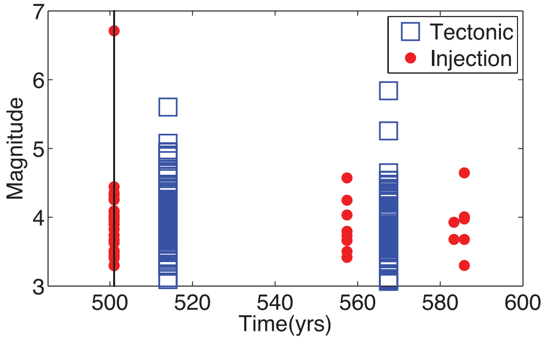

Figure 8. Seismicity recorded over a 100 yr period on the fault. Dots denote earthquakes from the catalogue where the injection takes place. The squares are from the catalogue where no injection takes place. The black line marks the time that injection takes place.

occurred during the injection. In Fig. 8 we see that the first, and largest earthquake in this catalogue is a M_w 6.7 event. The event occupies an area of 20 km by 15 km, has an average slip of 1.5 m and a maximum slip of 4.1 m which compares favourably to the M_w 6.7 Northridge which covered an area of 15 km by 20 km, had an average slip of 1.3 m and a maximum slip of 3 m (Wald *et al.* 1996). A more detailed discussion on this point is provided in the Appendix. In the control catalogue the first earthquake occurs 13 yr later (i.e. year 514) compared with the catalogue containing the injection. This variation between the timing of the two earthquake sequences can be explained in terms of clock advance. Perfettini *et al.* (2003) found, albeit for faults whose frictional parameters were smooth, that positive Coulomb stress changes of 1–10 bars cause clock advances of earthquakes by between 1 and 10 yr for earthquakes which are not nearing the end of their seismic cycle. The seismicity induced during the injection supports this observation. Stress perturbations due to the injection cause a 3.5 bar in Coulomb stress change on the fault and induce earthquakes in year 501, an advance of 13 yr. Additionally, however, our simulations yielded a change in the nature of the seismicity in terms of a change in the size of the event. In the control catalogue the biggest earthquake is a M_w 5.6 (see squares in Fig. 8) while the injection catalogue contains a M_w 6.7. In fact, the M_w 6.7 earthquake observed in the injection catalogue is the largest recorded in either of the catalogues over the subsequent 300 yr. This change in magnitude is not comparable to Perfettini *et al.* (2003) results as their model primarily produces events with very similar sizes due to the smooth nature of the frictional parameters in their seismogenic zone. Thus these results suggest that the idea of clock advance may be of limited use in a complex natural fault system that is characterized by material complexity both on individual faults and in stress interactions between complex networks of faults, stress perturbations may change the entire future of a given earthquake series.

Comparing the two seismic catalogues in Fig. 8 over 100 yr, we note that the injection catalogue hosts three further sequences of events which take place in years 557, 583 and 585 with maximum magnitudes of 4.5, 3.9 and 4.6, respectively. In the control catalogue, there are a total of two sequences during the same period, which occur in years 514 and 567, the largest earthquakes in these sequences are M_w 5.6 and M_w 5.8, respectively. The divergence between the two catalogues, both in terms of the timing and maximum magnitude of earthquake sequences highlights the strong affect that the small stress perturbations from the injection have on the fault, not only during and in the immediate aftermath of the injection, but permanently. This can be attributed to the non-linearity of the model system.

The effect of the injection is also clearly visible in the frequency–magnitude relationship of the seismicity. In the 100-yr period before the injection the fault generated a power-law distribution (see Fig. 4 and dotted line in Fig. 10). In the aftermath of the injection, there is a pronounced break in the power-law distribution due to the presence of the induced M_w 6.7 event. The size of the event induced by the injection relaxed the fault producing a subcritical frequency-size distribution (Steacy & McCloskey 1999) for the following 200 yr. This is apparent in Fig. 8 where the normalized frequency-magnitude distribution for two 100 yr periods after the M_w 6.7 event (i.e. years 501–601 and 601–701) are plotted against the dotted line denoting the best fit line for the scaling relationship for the 100 yr preceding the injection (i.e. 400–500 yr). Between years 501 and 601 we observe a lack of self-similar scaling followed by a noticeable shift back towards the frequency–magnitude distribution observed before the injection took place (i.e. the dotted line). The nature of this shift is similar to that observed by Heimpel (1997) where he observed an evolution towards a self similar scaling for a fault moving from a subcritical to critical state. Therefore while the timing of the seismic sequences and the maximum magnitude they contain has been permanently altered by the injection; the collective state of the fault system gradually returns to one of self-organized criticality due to on-going tectonic loading.

Note that this implies no contradiction with the earlier observation that the state of the fault is permanently changed. The precise timing, magnitude and slip distribution of future events are permanently altered but the global statistics of the sequence evolves back to a critical state which generates large events broadly consistent with the power-law distribution, even though they are not the same events which would have happened had the injection not occurred. That is, the energy perturbations to the fault (in the form of external stress perturbations caused by fluid injections in the case of this study) permanently alter the locations, timing and size of individual events in the fault. At the same time, viewing the collective behaviour of the fault (through the size-frequency distribution relationship) we can see that the fault returns to a critical state due to the continuous loading of elastostatic energy by the plate velocity (i.e. $V_{pl} = 35$ mm yr^{-1}). If we had used a smaller plate velocity in our models we would expect the fault to take longer to return to a state of criticality, if it was zero, the fault would never return to a critical state.

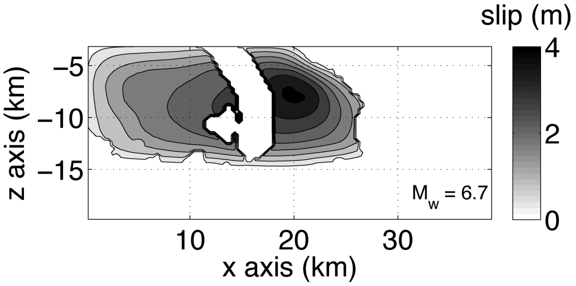

Figure 9. Slip distribution for the induced M_w 6.7 event. Below 15 km the velocity strengthening section of the fault means no coseismic slip extends into this zone. The near-vertical wedge in the slip distribution where no slip occurs (i.e. at 15 km along strike/*x*-axis) is due to a complex interaction between the rupture and the spatial variation of the frictional $a - b$ parameter causing it to act like a barrier to coseismic slip. The sharpness between barrier and seismic zone of the fault is probably due to the selection procedure used for determining whether a cell in the model is slipping seismically or not (i.e. the slip velocity of the cell *is* greater than 1 mm s^{-1}). Due to the continuity of slip either side of the barrier points to the barrier area experiencing a large slipping event during the earthquake, however it occurred at velocities less then 1 mm s^{-1}.

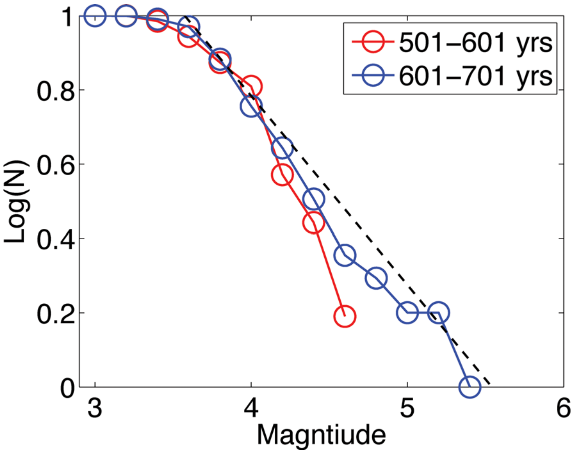

Figure 10. Frequency-size distribution for two 100 yr time periods on the fault. The red line is for the 100 yr just after the initial M_w 6.7 earthquake (i.e. year 501–601), the blue curve is for the earthquakes observed between year 601–701. The dotted black line is the best-fit line for the same distribution between year 400–500 (i.e. the 100 yr preceding the injection). Over time, the scaling relationship reverts back to the original condition on the fault just before the injection of near-criticality.

While the M_w 6.7 event does not rupture the entire seismogenic zone (see Fig. 9), the fault did not generate any earthquake bigger than this over a 1000-yr period (see Fig. 5). Therefore while it is conceivable that the fault could accommodate a larger earthquake (see theoretical approximations estimated in Model Setup), this would likely be extremely infrequent. The size of the earthquake generated by the injection is probably due to a combination of the size and duration of the stress perturbations caused by the injections as well as the timing of the injection relative to the naturally occurring seismicity on the fault. The actual magnitude of the M_w 6.7 event is primarily dependent on the size of the fault and state of the stress on it. The injection takes place when the fault is 70.4 per cent through its current seismic cycle (i.e. the previous seismic sequence was in year 470, the injection takes place in year 501 and the next seismic sequence to take place in year 514 if no injection occurs) therefore it has already accumulated a large amount of elastostatic energy. The rapid additional loading supplied by the injection (3.5 bar of Coulomb stress in 6.5 days) advanced the timing and increased the size of the next earthquake on the tectonically stressed fault. A proper investigation of these parameters (i.e. injection strength and duration, state of stress on the fault) and their sensitivity and the effect on the likelihood of inducing large earthquakes is required, however it is beyond the scope of this paper.

We have designed our numerical model so that it is not representative of any specific place or scenario. However, is it possible that the large earthquake generated in our numerical model could happen in reality? In purely tectonic settings, it is generally accepted that stress perturbations caused by one earthquake can trigger other large earthquakes [e.g. M_w 6.5 Big Bear (King *et al.* 1994), M_w 8.7 Nias (Nalbant *et al.* 2005)]. Fluid injection/extraction has been attributed to a series of M_w 7 events near the Gazli gas fields in Uzbekistan (Suckale 2010) and M_w 6.5 event in East Coalinga, California (McGarr 1991). Nicol *et al.* (2011) observed that the maximum induced magnitude scales with injected fluid volume which suggests that the maximum magnitude is boundless. In our numerical simulations the largest induced earthquake was a M_w 6.7 event. While we are uncertain if this is the largest earthquake the fault can host, it is an extremely rare event. Coupled with the observations of one earthquake triggering another in tectonic seismology implies that the generation of large earthquakes from the stress perturbations caused by fluid injection is possible and may ultimately be controlled by the fault size.

In our investigation, we used a fast plate velocity, which loaded the fault quickly resulting in a quasi-period recurrence time of 50 yr between seismic sequences and reloading period of 200 yr from the M_w 6.7 event. In terms of inducing earthquakes, the loading rate may be of little importance apart from controlling the recurrence time; it is the size of the structure and its closeness to failure that will affect an induced earthquake's size. It is now broadly accepted that the crust, and some of the faults in it, are likely to be in a critical state (Zoback *et al.* 2002) and therefore the possibility of inducing large earthquakes, however unlikely, is also possible.

5 CONCLUSION

Our numerical study showed that active faults near injection sites, while not being directly in contact with the injected fluids, could be greatly affected by stress perturbations caused by their presence. In our simulation, the injection induced a M_w 6.7 event which is entirely controlled by the fault and its previous tectonic loading; the injection simply triggers the release of this stored energy. The temporal advance for the forthcoming earthquake sequence is similar to the discussion of clock advance on a frictionally smooth fault. However, with a spatially heterogeneous frictional fault we observe variations in the size of the event that the external stress perturbation induced. Additionally, we find that the injection not only advanced the next sequence of earthquakes on the fault and varied their size; it also permanently altered the size and temporal occurrence of earthquakes on the fault. We find that the large induced earthquake temporally shifted the fault to a state of subcriticality but with continuous tectonic loading the fault regained a position of near self-organized criticality in the space of 200 yr.

It is vital that we emphasize the context of this study, which, if misunderstood, could raise significant concerns about the acceptability of economic fluid injection techniques. In this study we do not model any particular place or scenario so our results are not in any way useful in decision-making about any particular project. Instead, we set out to explore the theoretical possibilities concerning what the maximum magnitude might be and what might control it. Our results show that the fluid injection can trigger earthquakes whose size is dependent on the size of the fault not the injection and that these faults do not necessary need to be in the injection site. While it is beyond the scope of this study we have attempted some preliminary Monte Carlo simulations to estimate the probability and our results indicate that such tectonically triggered events will be extremely rare; the incorporation of the statistics of such low-probability events into risk management plans is likely to be challenging.

ACKNOWLEDGEMENTS

Comments by the editor E. Hauksson and two anonymous reviewers helped improve the manuscript. The authors acknowledge funding from a Griffith Geoscience Research Award of the Department of Communications, Energy and Natural Resources under the National Geoscience Programme 2007-2013 (Ireland).

REFERENCES

Ake, J., 2005. Deep-injection and closely monitored induced seismicity at paradox Valley, Colorado, *Bull. seism. Soc. Am.,* **95**(2), 664–683.

Baisch, S., Vörös, R., Rothert, E., Stang, H., Jung, R. & Schellschmidt, R., 2010. A numerical model for fluid injection induced seismicity at Soultz-sous-Forêts, *Int. J. Rock Mech. Mining Sci.,* **47**(3), 405–413.

Barbot, S., Lapusta, N. & Avouac, J.P., 2012. Under the hood of the earthquake machine: toward predictive modeling of the seismic cycle, *Science,* **336**(6082), 707–710.

Blanpied, M.L., Lockner, D.A. & Byerlee, J.D., 1991. Fault stability inferred from granite sliding experiments at hydrothermal conditions, *Geophys. Res. Lett.,* **18**(4), 609–612.

Cappa, F. & Rutqvist, J., 2012. Seismic rupture and ground accelerations induced by CO_2 injection in the shallow crust, *Geophys. J. Int.,* **190**(3), 1784–1789.

Dieterich, J., 1979. Modeling of Rock Friciton: 1. Experimental results and constituive equations, *J. geophys. Res.,* **84**(B5), 2161–2168.

Gallovič, F., 2008. Heterogeneous Coulomb stress perturbation during earthquake cycles in a 3D rate-and-state fault model, *Geophys. Res. Lett.,* **35**(21), doi:10.1029/2008GL035614.

Hanks, T. & Kanamori, H., 1979. A moment-magnitude scale, *J. geophys. Res.,* **84,** 2348–2352.

Heimpel, M., 1997. Critical behaviour and the evolution of fault strength during earthquake cycles, *Nature,* **388**(6645), 865–868.

Hillers, G., Ben-Zion, Y. & Mai, P., 2006. Seismicity on a fault controlled by rate- and state-dependent friction with spatial variations of the critical slip distance, *J. geophys. Res.,* **111**(B01403), doi:10.1029/2005JB003859.

King, G., Stein, R. & Lin, J., 1994. Static stress changes and the triggering of earthquakes, *Bull. seism. Soc. Am.,* **84**(3), 935–953.

Lapusta, N. & Liu, Y., 2009. Three-dimensional boundary integral modeling of spontaneous earthquake sequences and aseismic slip, *J. geophys. Res.,* **114**(B09303), doi:10.1029/2008JB005934.

Linker, M. & Dieterich, J., 1992. Effects of variable normal stress on rock friction: observations and constitutive equations, *J. geophys. Res.,* **97**(B4), 4923–4940.

Lisowski, M., Savage, J.C. & Prescott, W.H., 1991. The velocity field along the San Andreas fault in central and southern California, *J. geophys. Res.,* **96**(B5), 8369–8389.

Maillot, B. & Main, I., 1996. A lattice BGK model for the diffusion of pore fluid pressure, including anisotropy, heterogeneity, and gravity effects, *Geophys. Res. Lett.,* **23**(1), 13–16.

McCloskey, J., Nalbant, S. & Steacy, S., 2005. Indonesian earthquake: earthquake risk from co-seismic stress, *Nature,* **434,** 291.

McClure, M.W. & Horne, R.N., 2011. Investigation of injection-induced seismicity using a coupled fluid flow and rate/state friction model, *Geophysics,* **76**(6), WC181–WC198.

McGarr, A., 1991. On a possible connection between three major earthquakes in California and oil production, *Bull. seism. Soc. Am.,* **81**(3), 948–970.

Nalbant, S.S., Steacy, S., Sieh, K., Natawidjaja, D. & McCloskey, J., 2005. Seismology: earthquake risk on the Sunda trench, *Nature,* **435**(7043), 756–757.

Nicol, A., Carne, R. & Gerstenberger, M., 2011. Induced seismicity and its implications for CO2 storage risk, *Energy Procedia,* **4,** 3699–3706.

Okada, Y., 1992. Internal deformation due to shear and tensile faults in a half-space, *Bull. seism. Soc. Am.,* **82**(2), 1018–1040.

Perfettini, H. & Schmittbuhl, J., 2003. Shear and normal load perturbations on a two-dimensional continuous fault: 2. Dynamic triggering, *J. geophys. Res.,* **108**(B9), doi:10.1029/2002JB001805.

Perfettini, H., Schmittbuhl, J. & Cochard, A., 2003. Shear and normal load perturbations on a two-dimensional continuous fault: 1. Static triggering, *J. geophys. Res.,* **108**(B9), doi:10.1029/2002JB001804.

Press, W.H., Teukolsky, S.A. & Vetterling, W.T., 1992. *Numerical Recipes in Fortran 77,* Cambridge University Press, pp. 704–716. Cambridge, UK.

Qian, Y. & d'Humieres, D., 1992. Lattice BGK models for Navier-Stokes equation, *Europhys. Lett.,* **17**(6), 479–484.

Rice, J., 1993. Spatio-temporal complexity of slip on a fault, *J. geophys. Res.,* **98**(B6), 9885–9907.

Rice, J. & Ben-Zion, Y., 1996. Slip complexity in earthquake fault models, *Proc. Nat. Acad. Sci. USA,* **93,** 3811–3818.

Roeloffs, E., 1996. Poroelastic techniques in the study of earthquake-related hydrologic phenomena, *Adv. Geophys.,* **37,** 135–195.

Roy, M. & Marone, C., 1996. Earthquake nucleation on model faults with rate- and state-dependent friction: effects of inertia, *J. geophys. Res.,* **101**(B6), 13 919–13 932.

Ruina, A., 1983. Slip instablity and state variable friction law, *J. geophys. Res.,* **88**(B12), 10 359–10 370.

Scholz, C., 2002. *The Mechanics of Earthquakes and Faulting,* 2nd edn, Cambridge University Press, Cambridge, UK.

Seeber, L., Armbruster, J.G. & Kim, W.Y., 2004. A fluid-injection-triggered earthquake sequence in Ashtabula, Ohio: implications for seismogenesis in stable continental regions, *Bull. seism. Soc. Am.,* **94**(1), 76–87.

Steacy, S.J. & McCloskey, J., 1999. Heterogeneity and the earthquake magnitude-frequency distribution, *Geophys. Res. Lett.,* **26**(7), 899–902.

Stein, R., 1999. The role of stress transfer in earthquake occurrence, *Nature,* **402,** 605–609.

Suckale, J., 2010. Modertate-to-large seismicity induced by hydrocarbon production, *Leading Edge,* **29,** 310–319.

Toda, S., Stein, R., Richards-Dinger, K. & Bozkurt, S., 2005. Forecasting the evolution of seismicity in southern California: animations built on earthquake stress transfer, *J. geophys. Res.,* **110**(B05S16), doi:10.1029/2004JB003415.

Wald, D.J., Heaton, T.H. & Hudnut, K.W., 1996. The slip history of the 1994 Northridge, California, earthquake determined from strong-motion, teleseismic, GPS, and leveling data, *Bull. seism. Soc. Am.,* **86**(1B), S49–S70.

Wells, D.L. & Coppersmith, K.J., 1994. New empirical relationships among magnitude, rupture length, rupture width, rupture area, and surface displacement, *Bull. seism. Soc. Am.,* **84**(4), 974–1002.

Zheng, H. & Shu, C., 2006. A lattice Boltzmann model for multiphase flows with large density ratio, *J. Comput. Phys.,* **218,** 353–371.

Zoback, M.D., Townend, J. & Grollimund, B., 2002. Steady-state failure equilibrium and deformation of intraplate lithosphere, *Int. Geol. Rev.,* **44,** 383–401.

APPENDIX: RELATIONSHIP BETWEEN SYNTHETIC EARTHQUAKES AND ACTUAL EVENTS

Using a quasi-dynamic (QD) relationship between stress and slip rate rather than a fully dynamic one means that our QD model does not fully simulation the dynamic waves generated during an earthquake. Comparing QD with fully dynamic models Lapusta & Liu (2009) found that the QD simulations produced lower slips and stress drops per event relative to the fully dynamic equivalent simulation. We, therefore, do not expect our model to accurately model the actual earthquakes. However, on comparing the rupture area and average slip of our largest synthetic earthquake (i.e. the induced M_w 6.7 event discussed in the main body of this paper) we find that it compares favourably to the observed source dimensions of the 1994 Northridge M_w 6.7 earthquake. Our synthetic earthquake appears to have slightly larger source parameters due to the fact that we rounded down the magnitude from 6.748.

In Fig. A1 the source parameters for 200 events induced events from the QD model (i.e. the blue dots) are plotted against the empirically derived relationships between rupture parameters and magnitude (i.e. the dotted lines in both plots). Source parameters from the Northridge earthquake are plotted as stars. In Fig. A1, the rupture area of the synthetic earthquakes shows a similar trend to the *Wells and Coppersmith's* empirical relationship (Wells & Coppersmith 1994).

Using the same 200 events we compare the average slip with the rupture length in Fig. A2. The rupture length is estimated by assuming that the ruptured area per event is circular and therefore $L \approx \sqrt{\text{Area}/\pi}$. Eq. (14) shows that these two parameter are empircally related to each by a factor of $\Delta\sigma/G$, where $\Delta\sigma$ is the average stress drop and G is the shear modulus (Scholz 2002). There is a large amount of scatter in the

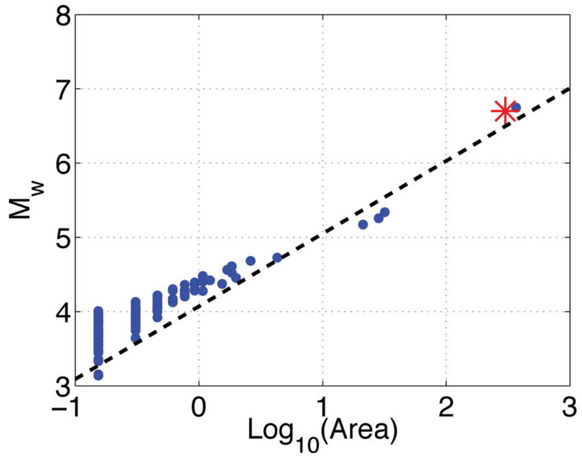

Figure A1. Rupture area of individual earthquakes plotted against the magnitude. The blue dots represent synthetic earthquakes generated by the QD model after the fluid injection (200 events are present). The red star represents the Northridge M_w 6.7 event [which had rupture are of 20 km by 15 km (Wald *et al.* 1996)]. The dotted line represents an empirical derived relationship between magnitude and rupture area: $M_w = 4.07 + 0.98\,\log(\text{Area})$ (Wells & Coppersmith 1994).

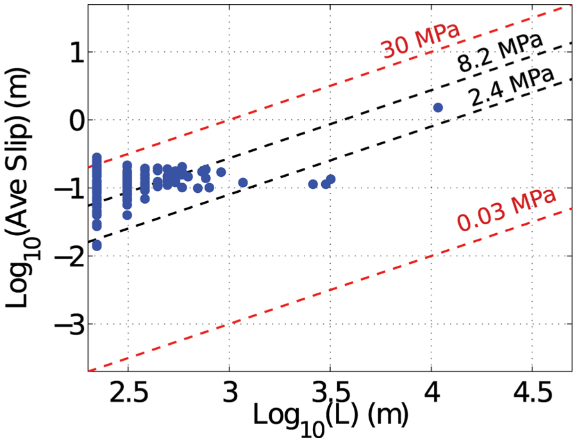

Figure A2. Plot of the average slip for 200 events generated after the fluid injection in the QD model against the length, L, of the earthquakes (blue dots). The length of the earthquakes are estimated by assuming that they are all circular events and therefore $L = \sqrt{A/\pi}$, where A is the area. By eq. (14) (i.e.$\delta = \frac{\Delta\sigma}{\mu} L$) the average slip ($\delta$), scales with rupture length (L) according to the average stress drop ($\Delta\sigma$). The black-dashed lines highlight this relationship using constant stress drops of 8.2 and 2.4 MPa; the red lines denote the same relationship for constant stress drops of 0.03 and 30 MPa.

data due to the frictional parameters, which vary spatially. This means that earthquakes have variable stress drops (see eq. 16) depending on the $b - a$ value of section of the fault ruptured seismically for that particular earthquake. Using the range of static stress drops calculated in Section 3 (Model Setup) for the seismogenic layer gives $\Delta\sigma = 8.2$ and 2.4 MPa. Taking $G = 30$ GPa we can produce a scaling relationship based on eq. (14) (black-dotted lines). While some of the earthquakes sit inside these lines, a portion of them do not. This could be due to a number of reasons: our assumption of a circular earthquake being inappropriate or that the stress drop in eq. (16) does not adequately describe the stress drop on the fault. The low average slip observed for the three earthquakes which fall below the lower of the two black lines is possibly due to these earthquakes rupturing into the velocity strengthening/aseismic zones on the fault. However, nearly all earthquakes fall within the generally acceptable stress drop range (i.e. 0.03–30 MPa), which are denoted by the red dashed lines.